

Corotating Dust Clumps Around Adolescent Low-Mass Stars: Four Years of TESS

LUKE G. BOUMA,^{1,*} RAHUL JAYARAMAN,² SAUL RAPPAPORT,² LYNNE A. HILLENBRAND,¹ AND GEORGE R. RICKER²

¹Department of Astronomy, MC 249-17, California Institute of Technology, Pasadena, CA 91125, USA

²MIT Kavli Institute and Department of Physics, 77 Massachusetts Avenue, Cambridge, MA 02139

(Received —; Revised —; Accepted —)

ABSTRACT

Complex quasiperiodic variables (CQVs) are low-mass pre-main-sequence stars with nearly periodic optical modulation. The modulation is likely induced by dust clumps in orbit at the Keplerian corotation radius. Here, we report new CQVs discovered in TESS data collected between July 2018 and Sep 2022, and analyze their variability. Our analysis of 65760 K- and M-dwarfs with $T < 16$ and $d < 150$ pc yielded 53 gold-standard CQVs. Most of these discoveries are new, and they include the brightest and closest examples of this class of object known ($T \approx 11$; $d \approx 20$ pc), as well as the most massive ($\approx 0.65 M_{\odot}$). A few objects are outliers among outliers; LP 12-502 for instance shows a “dip complex” with a period and total duration that are fixed over more than 1000 cycles, but which in detail shows anywhere from four to eight local minima per cycle. LP-502 also demonstrated drastic shape changes over less than one cycle, and at times displayed distinct superposed periods simultaneously. Broadly speaking, we find that none of the CQVs maintain a fixed light curve shape over timescales of more than a few hundred cycles – they are all *quasiperiodic*. We revisit the arguments for why transient corotating dust clumps are the most likely explanation, though there are other possibilities. In the future, we expect that our sample will help facilitate modeling and observational efforts aimed at understanding these objects, and connecting them to the broader contexts of star, disk, and exoplanet evolution.

Keywords: Weak-line T Tauri stars (1795), Periodic variable stars (1213), Circumstellar matter (241), Star clusters (1567), Stellar magnetic fields (1610), Stellar rotation (1629)

1. INTRODUCTION

All pre-main-sequence stars vary in optical brightness, and the origin of such variability is, in most cases, understood. Well-explored sources of optical variability include inhomogeneities on stellar surfaces such as starspots and faculae (Basri 2021), occultations by gas-rich circumstellar disks (Bodman et al. 2017), and, in geometrically favorable circumstances, eclipses by stars and planets (Winn 2010).

Data from K2 and TESS have yielded a new class of variable star whose root cause is only beginning to become clear: complex quasiperiodic variables (CQVs). These objects are identified phenomenologically using their optical light curves, which show quasiperiodic troughs that can be either sharp or broad, often superposed on smooth spot-like modulation (Stauffer et al. 2017, 2018; Zhan et al. 2019). Some CQVs show up to eight local minima (dips) per cycle; sharp peaks are common, but . Most CQVs are pre-main-sequence M-dwarfs without near-infrared excesses, with ages of ≈ 5 -150 million years (Myr), and rotation periods of at most two

days; they are observed to be $\approx 1\text{-}3\%$ of M-dwarfs younger than 100 Myr (Rebull et al. 2016; Günther et al. 2022). The dips can be chromatic, with a reddening law plausibly consistent with dust (Bouma et al. 2020; Günther et al. 2022; Koen 2023). And finally, while the dip shapes can “jump” between different depths and durations over less than one cycle, they more often evolve gradually, over tens to hundreds of cycles (e.g. Stauffer et al. 2017; Palumbo et al. 2022; Popinchalk et al. 2023).

A few competing explanations for what causes the complex quasiperiodic variability are shown in Figure 1, along with a few representative light curves. All young M-dwarfs are spotted, which produces flux variations over characteristic timescales of the rotation period, P_{rot} , and its half-harmonic, $0.5P_{\text{rot}}$. The observed dips occur over durations as short as $0.05P_{\text{rot}}$; a “starspot-only” scenario can be discarded for any object with sufficiently sharp dips (Stauffer et al. 2017; Koen 2021). The more likely scenarios invoke sharp geometries with material extrinsic to the stellar surface (e.g. Stauffer et al. 2017; Günther et al. 2022). In the “clump” scenario, opaque dust clumps orbiting near the Keplerian corotation radius eclipse the star (Stauffer et al. 2017; Sanderson et al. 2023). In the “prominence” scenario, long-lived condensations of plasma are trapped along the star’s

Corresponding author: Luke G. Bouma
luke@astro.caltech.edu

* 51 Pegasi b Fellow

magnetic field lines, also near corotation (Waugh & Jardine 2022). There is also a “screen” scenario, in which the inner wall of a quiescent circumstellar disk blocks a portion of the stellar surface to produce sudden dips whenever spots come into view (Zhan et al. 2019).

In our view, the arguments seem best established for the dust clump hypothesis (Sanderson et al. 2023). This is primarily because the prominence scenario lacks a mechanism for generating broadband opacity, and the screen scenario seems inconsistent with the degree of observed periodicity, and the lack of infrared excess. However, unambiguous evidence, for instance a spectroscopic detection of silicates during a CQV “dip”, has yet to be presented to confirm which scenario is correct.

CQVs have been challenging to understand because they have been both hard to discover and hard to characterize. Discoverability is tied to rarity: CQVs comprise about 1% of the youngest 1% of M-dwarfs (Rebull et al. 2018). Out of the millions of stars monitored by K2 and TESS, about 50 CQVs have been reported to date (Rebull et al. 2016; Stauffer et al. 2017, 2018; Zhan et al. 2019; Bouma et al. 2020; Günther et al. 2022; Popinchalk et al. 2023). The known CQVs are correspondingly faint; the initial K2 discoveries (Rebull et al. 2016; Stauffer et al. 2017) were M2-M6 dwarfs at distances $\gtrsim 100$ pc, yielding optical brightnesses of $V \approx 15.5$ to $V > 20$. This renders time-series spectroscopy at high resolution technically impossible, despite its potential utility in ruling between the models.

One way to help rule between the mechanisms is to therefore find bright and nearby CQVs, since these objects will be the most amenable to detailed photometric and spectroscopic analyses. To do this, in this work, we use 120-second cadence data acquired by TESS between July 2018 and Sep 2022 (Sectors 1-55; Cycles 1-4). We present our search methods in Section 2; and the properties of the resulting CQV catalog in Section 3. Open questions are discussed in Section 5, and we conclude in Section 6.

A point on nomenclature. CQVs have been called “transient and persistent flux dips”, “scallop shells”, “batwings”, (Stauffer et al. 2017) “complex rotators”, (Zhan et al. 2019; Günther et al. 2022; Popinchalk et al. 2023) and “complex periodic variables” (Koen 2023). The CQVs should not be conflated with “dippers”, which are classical T Tauri stars with infrared excesses whose optical variability is linked to obscuring inner disk structures and accretion hot spots (Cody et al. 2014; Robinson et al. 2021). At the risk of introducing yet another standard, we prefer a nomenclature that reflects how, when observed over timescales of more than tens of cycles, CQVs are never exactly periodic. Their shapes evolve, usually with some coherence timescale, similar to variability induced by surface inhomogeneities such as starspots. While the three-type classification scheme proposed by Stauffer et al. (2017) may indeed provide some helpful visual distinctions amongst CQV sub-classes, it seems likely that they are all explained by a single underlying phenomenon, and so we opt to refer to them by a single empirically descriptive name.

2. METHODS

2.1. Stellar selection function

We analyzed the “short” 120-second cadence data acquired by TESS between July 2018 and Sep 2022 (Sectors 1-55). Specifically, we used the 120-second cadence light curve products produced by the mission’s Science Processing and Operations Center at NASA Ames (Jenkins et al. 2016). While the TESS data products also include full frame images with cadences of 200, 600, and 1800 seconds, we limited our scope in this work for the sake of simplicity in data handling. In exchange, we lose in both completeness and homogeneity of the selection function. While TESS cumulatively observed $\approx 90\%$ of the sky for at least one lunar month between July 2018 and Sep 2022, the 120-second cadence data were acquired for only a pre-selected set of stars over Sectors 1-26, and then a guest-investigator driven set of stars over Sectors 27-55 (Fausnaugh et al. 2021).

To assess the completeness of the resulting 120-second cadence data that is the basis of this study, we cross-matched TIC8 (Stassun et al. 2018) against the Gaia DR2 point-source catalog (Gaia Collaboration et al. 2018). We opted for Gaia DR2 rather than DR3 because the base catalog for TIC8 was Gaia DR2, which facilitated a one-to-one crossmatch using the Gaia source identifiers. This exercise showed that for $T < 16$ M-dwarfs, the TESS 2-minute data are roughly 50% complete at ≈ 50 pc. At < 20 pc, $\gtrsim 80\%$ of the $T < 16$ M-dwarfs have at least one sector of short-cadence data; at > 100 pc, $\lesssim 10\%$ of such M-dwarfs have at least one sector of short-cadence data. Armed with this understanding, we then used our cross-match between Gaia DR2 and TIC8 to select our stars of interest, which we defined as stars with 120-second cadence TESS light curves that satisfied

$$T < 16 \quad (\text{Bright for TESS}) \quad (1)$$

$$G_{\text{BP}} - G_{\text{RP}} > 1.5 \quad (\text{Red stars only}) \quad (2)$$

$$M_G > 4 \quad (\text{Dwarf stars only}) \quad (3)$$

$$d < 150 \text{ pc} \quad (\text{Close stars only}), \quad (4)$$

for $M_G = G + 5 \log(\varpi_{\text{as}}) + 5$ the Gaia G -band absolute magnitude, ϖ_{as} the parallax in units of arcseconds, and a geometric distance d defined by inverting the parallax and ignoring any zero-point correction. This selection function includes dwarf stars later than spectral types of $\approx \text{K}6\text{V}$ (Pecaut & Mamajek 2013). The target sample therefore includes 65760 M-dwarfs and late-K dwarfs, down to $T < 16$ and out to $d < 150$ pc.

2.2. CQV discovery

Previous methods for finding CQVs have included visually examining stars known to be in young clusters (Rebull et al. 2016; Stauffer et al. 2017), and automatically flagging rapid rotators with a large number of strong Fourier harmonics (Zhan et al. 2019). The latter approach still requires visual vetting, since “stars with many Fourier harmonics” is a designation that includes objects such as eclipsing binaries or multiple stars blended into a single photometric aperture. In this work, we implemented a new search approach based on

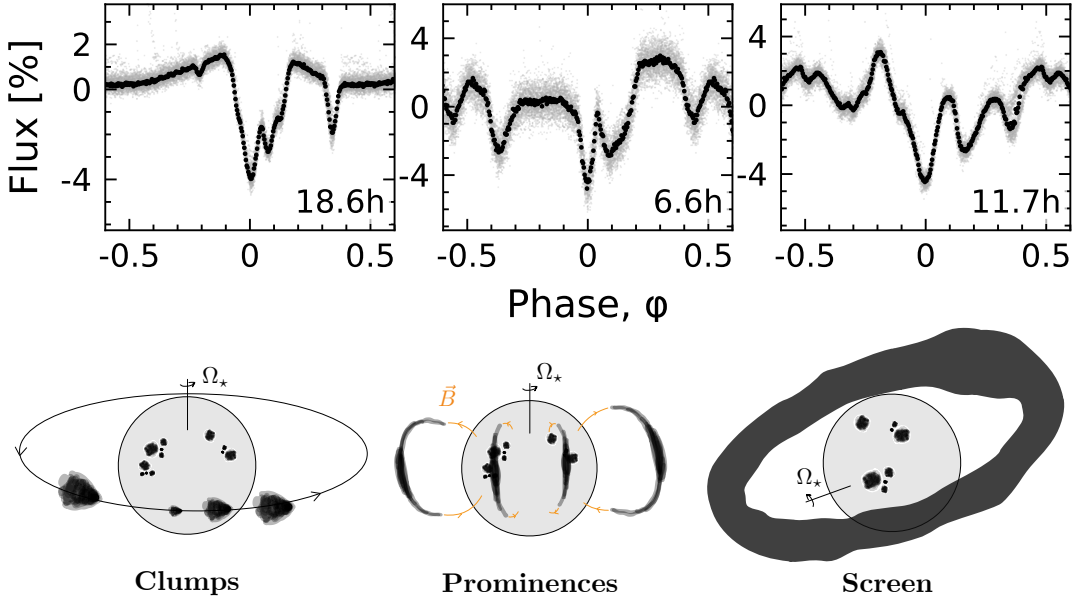


Figure 1. Complex quasiperiodic variables (CQVs): *Top:* Phase-folded TESS light curves of three CQVs. Each is stacked over one month. Gray are raw 2-minute data; black bins to 300 points per cycle. Periods in hours are in the bottom right of each panel. In order left-to-right, the objects are LP 12-502 (TIC 402980664; Sector 19), TIC 94088626 (Sector 10), and TIC 425933644 (Sector 28). *Bottom:* Plausible cartoon models for the phenomenon. The dust clump scenario seems most plausible, given the stability of the dips, the lack of observed infrared excesses, and the challenge of producing broadband opacity variations with only ionized hydrogen in the prominence scenario.

counting the number of sharp local minima in phase-folded light curves, while also using the previously tested Fourier approach. We applied these two search techniques independently.

2.2.1. Counting dips

The dip counting technique aims to count sharp local minima in phase-folded light curves. CQVs will preferably have at least three such minima in order to be distinct from false positives such as synchronized and spotted binaries (“RS CVn” stars).

For our dip-counting pipeline, we began with the PDC_SAP flux for each sector, removed non-zero quality flags, and normalized the light curve to one by dividing out its median value. We then flattened the light curve using a 5-day sliding median filter, as implemented in `wotan` (Hippke et al. 2019). On the resulting cleaned and flattened light curve, we ran a periodogram search, opting for the Stellingwerf (1978) phase dispersion minimization (PDM) algorithm implemented in `astrobase` (Bhatti et al. 2021) due to its shape agnosticism. If a period below 2 days was identified, we reran the periodogram at a finer grid to improve the accuracy of the period determination.

Once a star’s period P was identified, we binned the phased light curve to 100 points per cycle. To separate “sharp” local minima from smooth spot-induced variability, we then iteratively fit penalized splines to the wrapped phase-folded light curve, excluding points more than two standard deviations away from the local continuum (Hippke et al. 2019). The maximum number of equidistant spline knots per cycle is the parameter in this framework that controlled the mean-

ing of “sharp”—we allowed at most 10 such knots per cycle, though for most stars fewer knots were preferred based on an ℓ^2 -norm penalty.

We then identified local minima in the resulting residual light curve using the SciPy `find_peaks` utility (Virtanen et al. 2020), which is based on comparing adjacent values in an array. For a peak to be flagged as significant, we required it to have a width of at least $0.02P$, and a height of at least twice the point-to-point RMS. This latter quantity is defined as the 68th percentile of the distribution of the residuals from the median value of $\delta f_i \equiv f_i - f_{i+1}$, where f is the flux and i is an index over time.

To correctly identify local minima near the edges of the phased light curve, which usually would cover phases $\phi \in [0, 1]$, we in fact performed the entire procedure over a phase-folded light curve spanning $\phi \in [-1, 2]$, by duplicating and concatenating the ordinary phase-folded light curve. The free parameters we adopted throughout this analysis procedure, for instance the maximum number of spline knots per cycle, and how large and wide of a local minimum to consider a “true dip”, were chosen during a testing period based on their ability to correctly re-identify a large fraction (>90%) of known CQVs, while also being able to consistently reject common false positives such as rapidly rotating spot-induced variability and typical eclipsing binaries.

Overall, for a star to clear this process and to proceed to manual examination, we required that it have a peak PDM period below two days, and that it exhibited at least three sharp local minima (as algorithmically reported) in at least one observed TESS sector.

2.2.2. Fourier analysis

For the Fourier analysis, we followed Zhan et al. (2019).

TODO for Rahul or Saul: explain the approach, in a few paragraphs. Was the SAP_FLUX or PDCSAP used? etc.

2.2.3. Manual vetting

We visually assessed whether the objects found using the Fourier (Section 2.2.2) and dip-counting (Section 2.2.1) techniques were consistent with expectations for CQVs by assembling the data shown in Appendix A.

Broadly speaking, the most common false positives for both the Fourier and dip-counting techniques were eclipsing binaries, spot-induced variability from rapid rotators, and variability from neighboring, off-target stars. Typical false positive rates from our dip-counting pipeline were 5:1, with 368 unique stars flagged, and about 20% being labelled either “good” or “possible” CQVs; for the Fourier pipeline, the rate was X:Y, with ZZZZ unique stars flagged, and NN% being labelled “good” or “possible” CQVs.

2.3. Stellar properties

Ages—We estimated the stellar ages by making probabilistic spatial and kinematic associations between the CQVs and known clusters in the solar neighborhood. For most stars in our sample, we did this using BANYAN Σ (Gagné et al. 2018).¹ This algorithm calculates the probability that a given star belongs to one of 27 young clusters (or “associations”) within 150 pc of the Sun, by modeling the clusters as multivariate Gaussians in 3-D position and 3-D velocity space. We used the Gaia DR2 sky positions, proper motions, and distances to calculate the membership probabilities. BANYAN Σ in turn analytically marginalizes over the radial velocity dimension. The probabilities returned by this procedure are qualitatively useful, but we emphasize that they are quantitatively dubious due to the non-Gaussian nature of most groups within the solar neighborhood (see e.g. Kerr et al. 2021, Figure 10).

For a few cases where BANYAN Σ yielded ambiguous results, we consulted the meta-catalog of young, age-dated, and age-dateable stars within a kiloparsec from Bouma et al. (2022), and also searched the local volume around each star for co-moving companions.²

Effective temperatures, radii, and masses—We determined the stellar effective temperature and radii through SED fitting; we then estimated the masses by interpolating against the PARSEC v1.2S models (Bressan et al. 2012; Chen et al. 2014).

For the SED fitting, we used astroARIADNE (Vines & Jenkins 2022). Specifically, we adopted the “BT-Settl” stellar atmosphere models (Allard et al. 2012) assuming the Asplund et al. (2009) solar abundances, and the Barber

et al. (2006) water line lists. The broadband magnitudes we considered included $GG_{\text{BP}}G_{\text{RP}}$ from Gaia DR2, V_{gr} from APASS, JHK_{S} from 2MASS, r_{iz} from Pan-STARRS1, SDSS r_{iz} , and the WISE 1-2 passbands. We specifically omitted UV flux measurements to avoid biasing our fit with any possible chromospheric UV excess. astroARIADNE compares the measured broadband flux measurements against pre-computed model grids, and by default fits for six parameters: $\{T_{\text{eff}}, R_{\star}, A_{\text{V}}, \log g, [\text{Fe}/\text{H}], d\}$. The distance prior is drawn from Bailer-Jones et al. (2021). The surface gravity and metallicity are generally unconstrained. And finally, given our particular use-case, we assumed the following priors for the temperature, stellar size, and extinction:

$$T_{\text{eff}}/\text{K} \sim \mathcal{N}(3000, 1000), \quad (5)$$

$$R_{\star}/R_{\odot} \sim \mathcal{T}_{\text{N}}(0.5, 0.3, 0.1, 1.5), \quad (6)$$

$$A_{\text{V}}/\text{mag} \sim \mathcal{U}(0, 0.2), \quad (7)$$

for \mathcal{N} the Gaussian and \mathcal{U} the uniform distributions, and $\mathcal{T}(\mu, \sigma, a, b)$ a truncated normal distribution with mean μ , standard deviation σ , and lower and upper bounds a and b . Using Dynesty (Speagle 2020), we statically sampled the posterior probability assuming the default Gaussian likelihood, and set a stopping threshold of $d\log Z < 0.01$, where Z denotes the evidence.

With the effective temperatures and stellar radii from the SED fit, we then estimated the stellar masses by interpolating against the PARSEC isochrones (v1.2S Chen et al. 2014). The need for models that incorporate some form of correction for young, active M-dwarfs is well-documented (e.g. Stassun et al. 2012; David & Hillenbrand 2015; Feiden 2016; Somers et al. 2020). Plausible explanations for anomalous M-dwarf colors and sizes relative to model predictions include star starspot coverage (e.g. Gully-Santiago et al. 2017), and potentially incomplete line lists (e.g. Rajpurohit et al. 2013). In the PARSEC models, Chen et al. (2014) performed an empirical correction to the temperature–opacity relation drawn from the BT-Settl model atmospheres, in order to match observed masses and radii of young eclipsing binaries. This is sufficient for our purpose of estimating accurate stellar masses. Given our observed $\{\tilde{T}_{\text{eff}}, \tilde{M}_{\star}, \tilde{t}\}$, and approximating their uncertainties as Gaussian $\sigma_{\tilde{T}_{\text{eff}}}, \sigma_{\tilde{M}_{\star}}$, and $\sigma_{\tilde{t}}$, we evaluate a distance d between our observations and any model PARSEC grid-point $\{T_{\text{eff}}, M_{\star}, t\}$ as

$$d^2 = \left(\frac{\tilde{T}_{\text{eff}} - T_{\text{eff}}}{\sigma_{\tilde{T}_{\text{eff}}}} \right)^2 + \left(\frac{\tilde{M}_{\star} - M_{\star}}{\sigma_{\tilde{M}_{\star}}} \right)^2 + \left(\frac{\tilde{t} - t}{\sigma_{\tilde{t}}} \right)^2, \quad (8)$$

in order to assign equal importance to each dimension. The preferred model mass is then one that minimizes this distance, and is quoted in Table ??.

3. RESULTS

3.1. CQV catalog

Table ?? lists the 70 CQVs identified by our search, along important physical and observational properties. 53 objects

¹ https://github.com/jgagneastro/banyan_sigma, git commit 394b486

² <https://github.com/adamkraus/Comove>, git commit 278b372

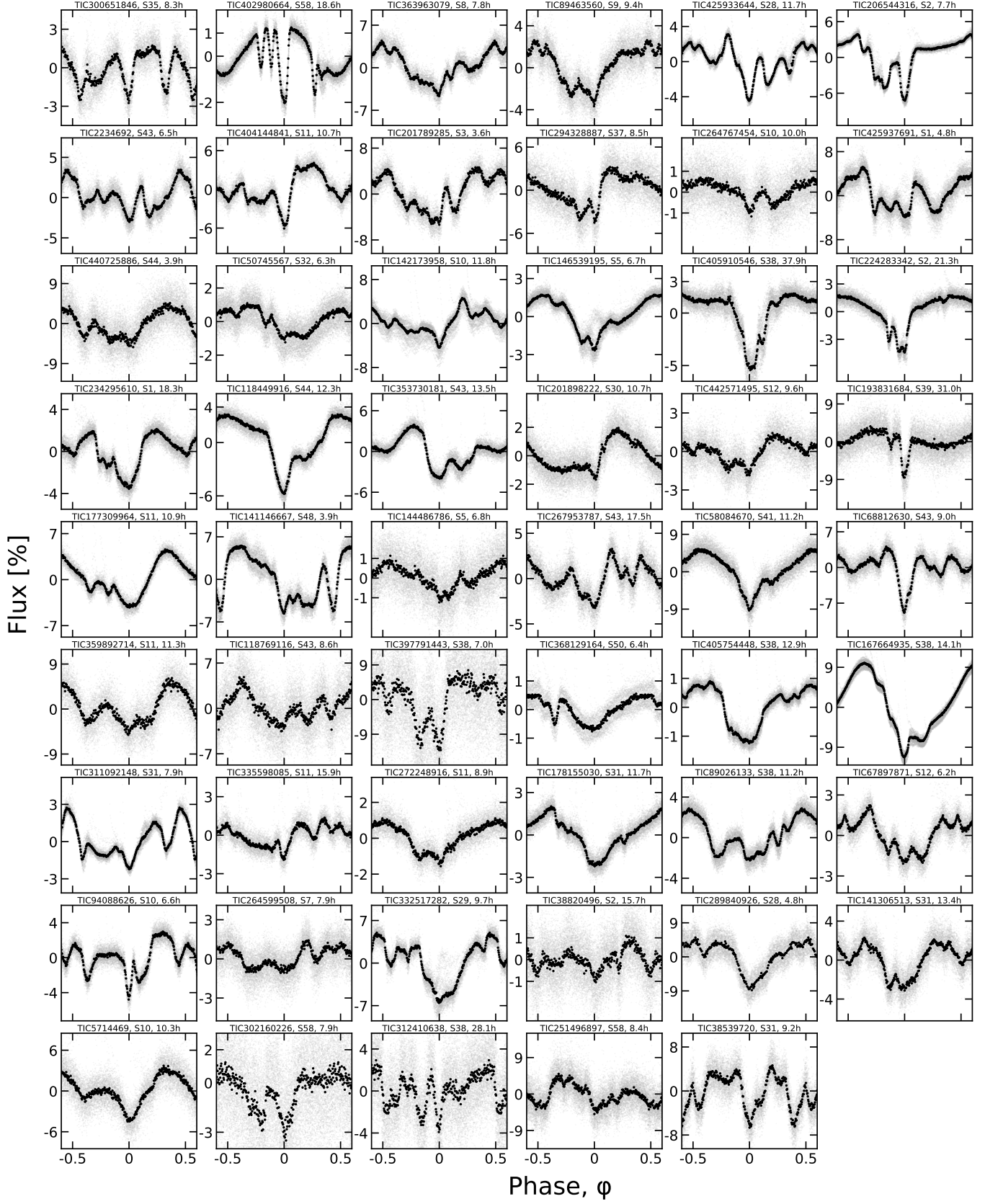


Figure 2. CQVs found in the TESS 2-minute data. Phased TESS light curves over one month are shown for 53 CQVs. Gray are raw 2-minute data; black bins to 300 points per cycle. Each panel is labelled by the TIC identifier, the TESS sector number, and the period in hours. Objects are ordered such that sources with the most TESS data available are on top (see Section 3.1).

demonstrate what we view as unambiguous characteristics of the CQV phenomenon in at least one TESS sector, and we refer to these as the “gold sample”. The remaining 17 CQV candidates were ambiguous (in our view), and their variability might be caused by say, multiple starspot groups. Additional data from TESS or other instruments can help resolve their classification; in Section 3.3 below for instance we discuss a few cases in this ambiguous sample that are probably dippers.

The mosaic in Figure 2 shows phased light curves for the 53 bona fide CQVs. The objects are sorted first in order of the number of TESS 120-second cadence sectors in which they clearly demonstrated the CQV phenomenon, and secondarily by descending brightness. The objects at the top therefore have the most 120-second cadence data. The top five objects by this metric are TIC 300651846 ($T=13.5$, 12 sectors); TIC 402980664 ($T=11.1$, 7 sectors); TIC 89463560 ($T=13.5$, 5 sectors); TIC 363963079 ($T=12.9$, 5 sectors); and TIC 294328887 ($T=14.2$, 4 sectors). The brightest five CQVs span $9.3 < T < 11.1$; the faintest five span $14.5 < T < 15.0$. The fastest five have periods spanning $3.6 \text{ hr} < P < 6.2 \text{ hr}$, while the slowest five span $27 \text{ hr} < P < 38 \text{ hr}$.

In terms of the light curve shapes, Figure 2 shows a broad range of variability, with anywhere from two to eight local minima per cycle. Some stars show relatively ordinary modulation during one continuous portion of the phased light curve, and highly structured modulation in the remainder of the cycle (e.g. TIC 206544316, TIC 224283342, TIC 402980664). Others show structured modulation over the entire span of a cycle (e.g. TIC 2234692, TIC 401789285, TIC 425933644, TIC 142173958). Others still show some mix between these two modes.

A small number of objects at first glance seem reminiscent of eclipsing binaries, for instance TIC 193831684 or TIC 5714469. In the few such cases, we believe that that are unlikely to be eclipsing binaries due to additional coherent variations in the light curves that are distinct from any binary phenomenology of which we are aware.

3.2. Ages

Of our 70 confirmed and candidate CQVs, 67 were confidently associated with a nearby moving group or open cluster using BANYAN Σ . The relevant groups are listed in Table ??; their ages span $\approx 5\text{-}150 \text{ Myr}$. The most prodigious groups were Sco-Cen, Tuc-Hor, and Columba. The yield in Sco-Cen (LCC / UCL / USco) is not surprising, since Sco-Cen contains the majority of pre-main-sequence stars in the solar neighborhood. The absence of CQVs in IC 2602 and IC 2391 can be understood by those clusters being beyond 100 pc, where the completeness of the TESS 120-second cadence data is below 10%; based on the abundance of CQVs in the 40 Myr Tuc-Hor and Columba, the similarly-aged IC 2602 and IC 2391 clusters should show a large number of CQVs in the TESS full frame image data.

Of the 3 stars for which BANYAN Σ did not find any association, one (TIC 302160226) is a member of α Per ($t \approx 86 \pm 16 \text{ Myr}$; Meingast et al. 2021; Boyle & Bouma 2022).

For the other two (TIC 58084670 and TIC 141146667), we are convinced of both their CQV status and their youth, but we were not able to confidently associate either star with any young groups. Both objects were noted as being in the “diffuse” Class III YSO population near the Sun by Kerr et al. (2021). That diffuse population may contain kinematic structures that have yet to be unravelled. However, the absence of obvious young, co-moving stars within $\Delta r = 40 \text{ pc}$ and $\Delta v = 3 \text{ km s}^{-1}$ of our two CQVs suggest that they may have “run away” from their birth locations.

The CQV phenomenon persists at least up to 150 Myr. Our catalog includes three $\approx 150 \text{ Myr}$ old AB Dor members (TIC 288344202, TIC 332517282, and TIC 368129164), a $\approx 112 \text{ Myr}$ old Pleiades member (TIC 440725886; Cantat-Gaudin et al. 2020), and a similarly-aged Psc-Eri member (TIC 38539720; Ratzenböck et al. 2020). To our best knowledge, TIC 332517282 was the previous record-holder for oldest-known CQV (Zhan et al. 2019; Günther et al. 2022); at least one unambiguous case (EPIC 211070495) and a few other candidates were also previously known in the Pleiades (Rebull et al. 2016). While we expect to have been sensitive to CQVs in the nearby Hyades ($\approx 700 \text{ Myr}$), again due to the specifics of the TESS 120-second selection function, we do not know at this time whether we would have been sensitive to such stars.

Finally, six CQVs were identified in the recently confirmed Argus association (Zuckerman 2019). This serves as an indirect line of evidence supporting the reality, and youth, of that group.

3.3. Infrared excesses

As is typical for CQVs (Stauffer et al. 2017), most CQVs in our catalog did not show infrared excesses in the WISE1-4 bands. Visually inspecting the SEDs, we labelled two objects as having “good” infrared excesses (both W3 and W4), and three as “possible” infrared excess.

The two “good” IR excesses were TIC 193136669 (TWA 34) and TIC 57830249 (TWA 33). Both are in the TW Hydrae association ($\approx 10 \text{ Myr}$), and have “long” periods of 38 hr and 44 hr respectively. In our initial labelling, we labelled both as “maybe” CQVs because the dips in their light curves did not show the rigid periodicity typical of CQVs; their periods were also relatively long. After labelling them, we learned that TIC 193136669 has a cold molecular disk based on observed 1.3 mm continuum emission and resolved Keplerian $^{12}\text{CO}(2-1)$ emission (Rodriguez et al. 2015). It has also been labelled a dipper by Capistrant et al. (2022); we agree with their designation, but nonetheless leave it in our catalog as an indication of possible ambiguities in our search process. TIC 57830249 (TWA 33) also has previously detected 1.3 mm continuum emission (Rodriguez et al. 2015), suggestive of cold dust grains being present. It therefore probably also a dipper that snuck its way into our “maybe” pile.

Our three “possible” infrared excesses were TIC 405910546, 289840926, and 244161191. After a literature search, we concluded that none have clear evidence

for the presence of a disk. TIC 405910546, in LCC, shows a unique TESS light curve, reminiscent of a $P=38$ hr singly-eclipsing binary, except with additional substructure during each eclipse that resembles the CQV phenomenon more than any other variability of which we are aware. TIC 289840926 (β Pic moving group, $P=4.8$ hr), show what we believe is a clear CQV signals, but has no definitive evidence for a large, dusty disk. TIC 244161191 (hilariously, TOI-278), in Columba, also has no definitive evidence for a large disk. It is however “multi-periodic”—in addition to the 7.17 hr CPV signal, there is a superposed 8.39 hr sinusoidal signal, probably from an unresolved binary neighbor.

Comparing these results against the backdrop of our increasing understanding of dippers (e.g. Cody et al. 2014; Ansdell et al. 2016; Robinson et al. 2021; Capistrant et al. 2022), it is clear that the loss of an infrared excess is associated with strong changes in a star’s optical variability. It is not unreasonable to imagine connections between CQVs and dippers: both classes of object can show transient flux dips that are relatively narrow in duration. Such dips are probably caused by clumps of dust. However the CQV dips are typically *i*) more periodic and *ii*) less deep than those of dippers, and *iii*) they display far less transience over timescales of a few to tens of cycles. At a population level, the CQV stars are also older. A shared mystery between the CQVs and dippers, in our own estimation however, is the exact mechanism that produces the *narrowness* of the dust clumps in certain cases. It is not unreasonable to imagine a similar mechanism operating for both types of object, tied perhaps to a shared magnetic topology, or perhaps to a preference for dust to insipral to the star in clumps from tidally disrupted infalling bodies.

4. CQV EVOLUTION

4.1. Evolution over two year baseline

Figure 3 shows “before” and “after” views of 21 CQVs for which observations were available at least two years apart. Of the 21 CQVs for which such a baseline was available, 5 showed obvious signs of the phenomenon in one sector, and marginal or non-existence signs in the other. We emphasize that the periods themselves were all stable to $<0.1\%$. Broadly speaking, this shape evolution suggests that CQVs have a duty cycle of $\approx 75\%$.

4.2. Evolution over adjacent sectors, & LP 12-502

4.2.1. LP 12-502 observations

While many CQVs had multiple sectors of adjacent or nearly-adjacent data LP 12-502 (TIC 402980664; $d=21$ pc, $J=9.4$, $T=11.1$) stood out as an outlier among the CQV class. Figure 4 shows all available data from Sectors 18, 19, 25, 26, 53, 58, and 59; the star was observed at 120-second cadence whenever it was observable by TESS. Figure 5 shows the same data, grouped into successive TESS orbits spanning half a lunar month each. Measuring the PDM peak period over each sector independently yielded an average $\langle P \rangle = 18.5560$ hr, with a difference between the maximum

and minimum sector-level period of about one minute. Based on this range, the period is therefore stable to at least one minute (± 0.017 hr) over the three year baseline. However, in detail, a period shift of ± 1 minute yields major phase drifts over the 3 year baseline; that time interval corresponds to roughly 1/1000th of a period; we have observed 1500 cycles. The achievable period precision, σ_P , can be estimated as

$$\sigma_P = \frac{\sigma_\phi P}{N_{\text{baseline}}}, \quad (9)$$

for N_{baseline} the number of cycles in the observed baseline and σ_ϕ the phase precision with which any one feature (e.g. a dip) can be tracked. Assuming $\sigma_\phi \approx 0.01$ yields an expected period precision $\sigma_P \approx 0.45$ sec $\approx 1.2 \times 10^{-4}$ hr. By visually fine-tuning over a grid in period, we eventually found $P = 18.5611 \pm 0.0001$ hr, which seems to track certain features in the LP 12-502 light curve over its entire baseline.

What features are observed? For the first 64 cycles, the star shows a pattern reminiscent of a (bizarre) eclipsing binary, with four obvious dips, that we dub dips {1,2,3,4} at phases $\{-0.28, -0.08, 0, 0.25\}$ respectively. Over cycles 0 to 64, the depth of dips 1 and 3 remain roughly fixed. However dip 4 *decreases* in depth by about 2%, while dip 2 *increases* in depth, by about the same amount. During cycles 48–64, it also seems that a fifth dip may be emerging, in the main “large” dip group.

There is then a 6-month (184 cycle) gap out to Cycles 248–315, which show two intricately structured dip complexes, plus a single (leading) dip. The single leading dip is present at roughly the same phase as in cycles 0–64; we believe they are the same struture. Along a similar line of logic, it seems plausible that the first “dip complex” during cycles 248–264 represents an evolution of the initial complex seen during cycles 0–64, though with greatly reduced depth. During cycles 266–310, a moving local minimum develops between the two complexes; this feature is best visualized on the river plots.

However, the second dip complex during cycles 248–315 is perhaps the most intricate. During e.g. cycles 283–298, this single complex clearly shows six local minima. The deepest dip is very sharp: it shows a flux excursion of 3.5% over about 22 minutes ($0.02 P$), which is the steepest slope exhibited anywhere in this object’s remarkable dataset. After the sharp dip, there is a roughly exponential fall-off spanning about a quarter of a period, punctuated by coherent local minima and maxima. The sharp leading dip only decreases in its sharpness during cycles 299–315, during a sudden state-switch at BTJD 2030.7, which happens immediately during a flare. (And therefore which is likely caused by the flare!) To our best knowledge, this type of behavior has not yet been observed on any comparable object.

Finally, sectors 53–58 (cycles 1233–1481) showed between four and six dips per cycle, at various times. Some dips remain stable in depth and duration over this five month interval. Other dips grow, like the one at $\phi = +0.06$ between cycles 1499 and 1481. Other dips, such as the one at $\phi = +0.12$ in cycles 1233–1264, disappear entirely. The most dramatic state switch occurs during cycles 1233–1247, when a large

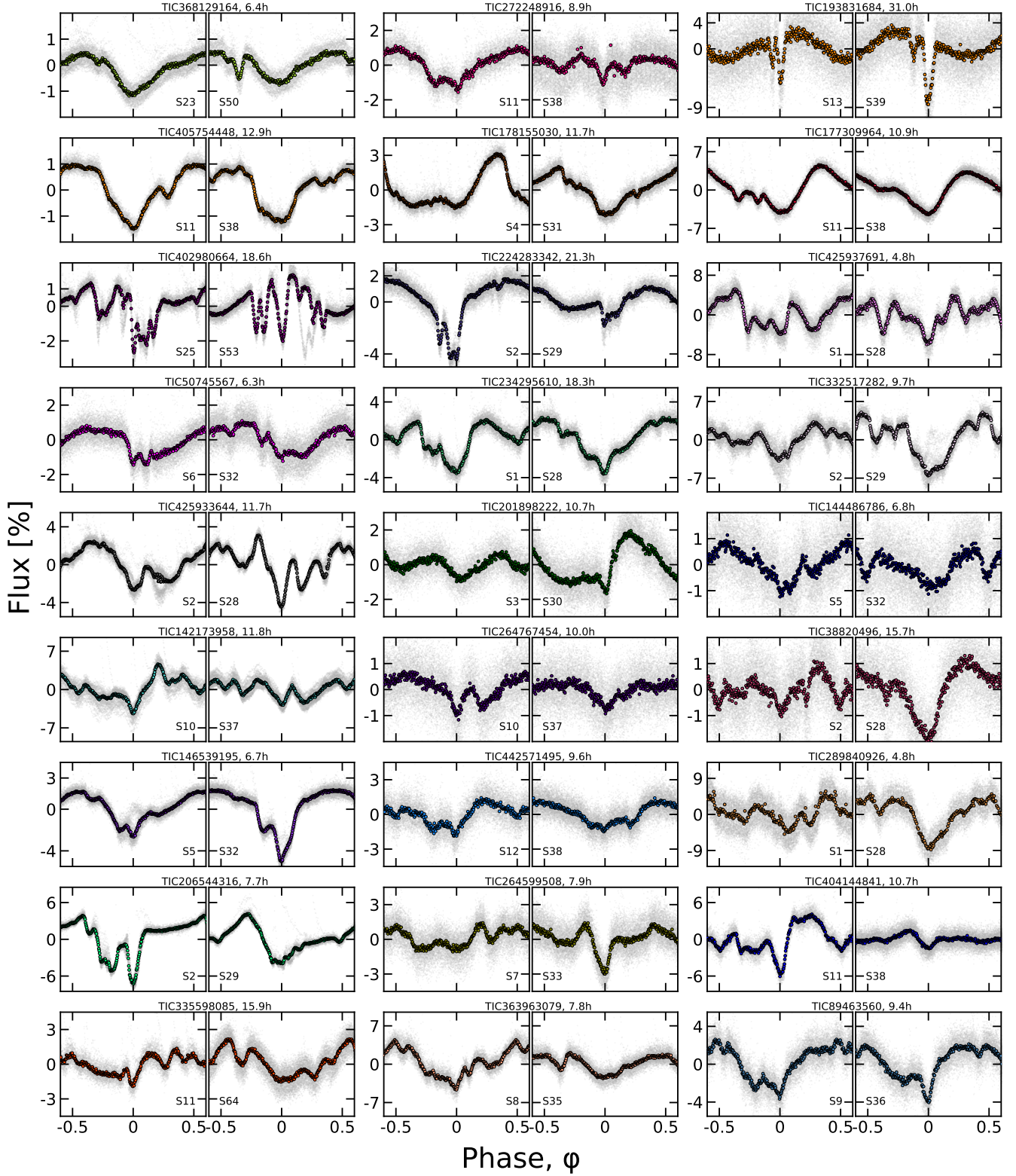


Figure 3. CQVs keep their periods but change their shapes. 32 of our 53 CQVs from Figure 2 had 120-second cadence TESS data available for a baseline of at least two years; the 27 brightest are shown here. Each panel shows one sector of TESS data, and is phased to its deepest minimum in flux. Each panel's title shows the TIC identifier and approximate period in hours. Text insets show the TESS sector numbers, which generally span two years, or at least 1,000 cycles. The vertical scale is fixed across sectors to clarify shape changes.

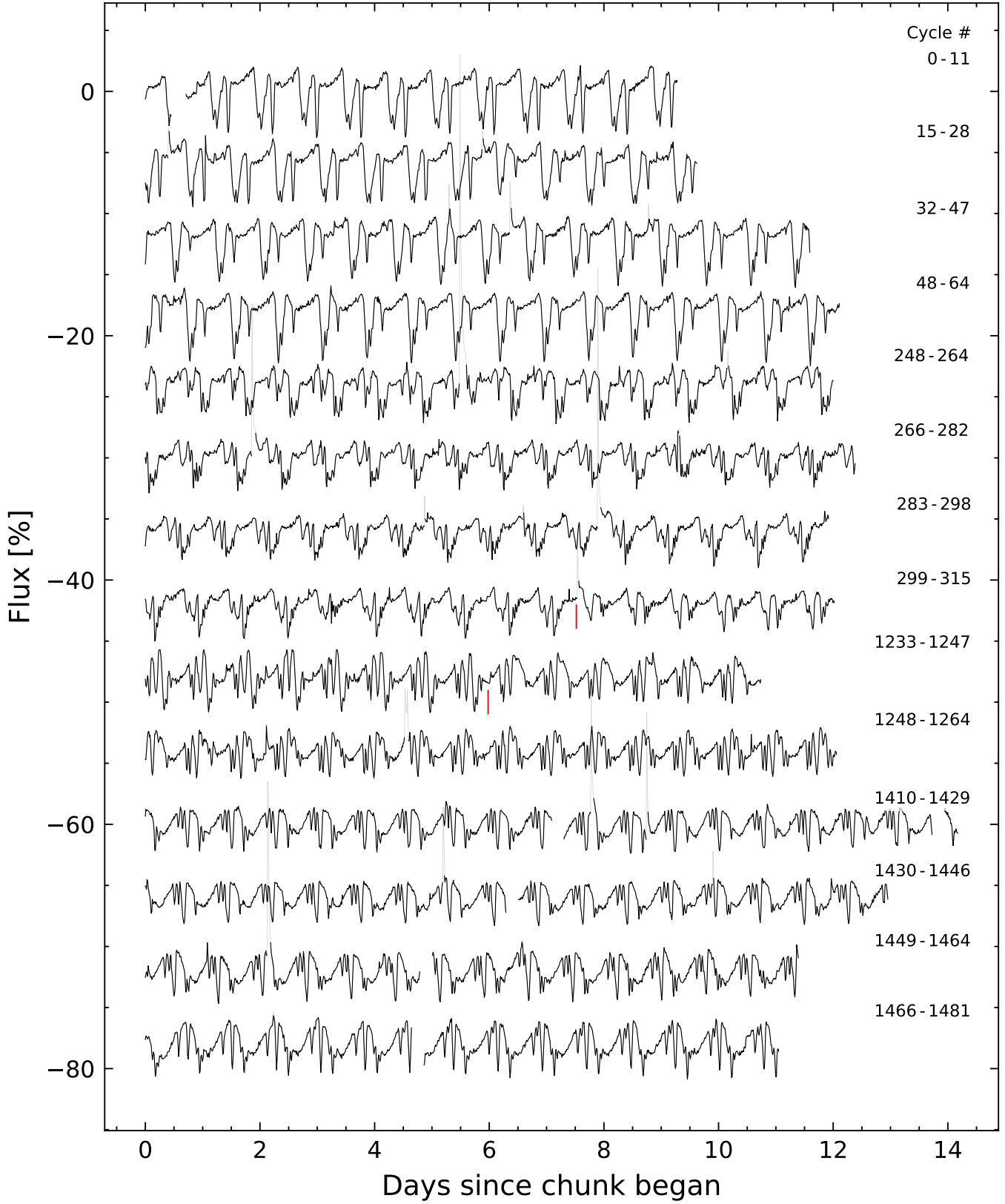


Figure 4. LP 12-502 (TIC 402980664) light curve, where each time chunk represents one TESS orbit. Data were acquired in Sectors 18-19, 25-26, 53, and 57-58. Flares are drawn in gray. The red vertical lines highlight apparently instantaneous state changes in the shape of the dip pattern. The light curve is binned to 15-minute intervals so that there are 96 points per day. Data gaps with more than one missing 15-minute cadence appear in white.

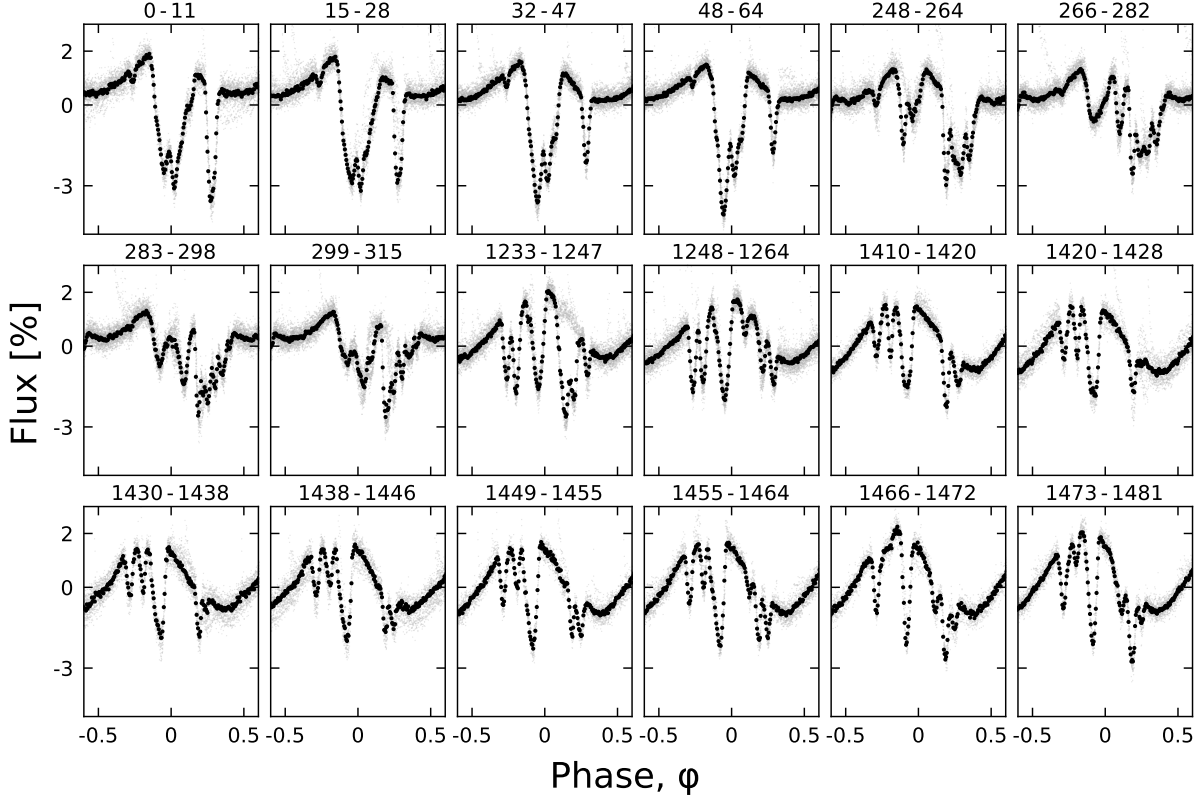


Figure 5. Evolution of LP 12-502 ($P=18.6$ h) at fixed period and epoch over three years. Each panel shows one (stacked) TESS orbit; small text denotes relative cycle number. There are 200 binned black points per cycle. The TESS pointing law dictates time gaps; larger gaps tend to yield larger shape changes. The dips usually evolve over tens to hundreds of cycles. However cycles 1233-1264 show a dip that “switched” from a depth and duration of 3% and 3 hr to 0.3% and 1 hr over less than one cycle.

dip “switches” from a depth of 3% and duration of 3 hours to a depth of 0.3%, and a duration of 1 hour.

4.2.2. LP 12-502 interpretation

DIPS CAN DISAPPEAR INSTANTANEOUSLY—The state switches shown in cycles 1233-1264 and 299-315 reveal that the dips can be *independent* and *additive*. They also show that although dip depth is generally not preserved over a state switch, *ingress time* usually is conserved. In other words, throughout cycles 1233-1264, there are three local minima between phases of 0 and 0.3. They all have identical ingress times. The shape change during the transition strongly suggests that it was simply the leading dip that “turned off”, while the trailing two dips remained fixed. The state switches during cycles 299-315 and 248-264 share the same characteristic: it is always the *leading* dip of a complex that “switches off”, leaving the trailing dips in its wake.

DIPS GROW MORE SLOWLY—Although there are a few instances in which we observe dips to “switch off” over less than one cycle, dip growth seems to happen more slowly. For instance, the dip that grows between phase 0 and 0.1 between cycles 260-290 begins to become visible around BTJD 1993.2, and grows in depth by about 2% over about six cycles, to become easily detectable by eye by BTJD 1997.7. The evolution of this particular dip is most clear in the river

plots. The evolution of the latter dip group in cycles 1410-1481 is another example of this slow mode of dip growth.

DIP ASYMMETRIES—The observed asymmetries include both sharp leading ingresses (e.g. for the main cycle 248-315 dip complex), and also extended ingresses with relatively sharper *egresses* (e.g. the deepest feature during cycles 1420-1464). Some dips do not show detectable asymmetry at all.

The asymmetry is an important characteristic because it can help diagnose the optical depth of the occulting material as a function of orbital phase angle. Sharp leading edges with trailing exponential egresses for instance have been previously seen for transiting exocomets and disintegrating rocky bodies (e.g. Rappaport et al. 2012; Brogi et al. 2012; Vanderburg et al. 2015; Zieba et al. 2019). We discuss this possibility below.

DIP DURATIONS—The shortest timescale that any of the *individual* dips seem to occur over is $\approx 0.07 P$, or about 1.3 hours. For a $M_\star = 0.25 M_\odot$, $R_\star = 0.5 R_\odot$ star, the characteristic timescale T_{dur} for the transit of a point-source over the stellar equator at $P = 18.6$ hours is also $0.07 P$. This means that while some of the LP 12-502 dips are sufficiently long to require structures that are extended in orbital azimuth, some are short enough that their durations are consistent with point sources.

DIP PERIODS—Most of the LP 12-502 dips recur with a period of $P = 18.5611 \pm 0.0001$ hr. However the river plots reveal multiple distinct periodicities in the light curve for specific dips. For instance, in sectors 25-26, the local minimum that develops around cycle 262 has a period faster than the mean period by $\approx 0.1\%$, while some of the trailing local minima in the main dip complex have periods slower than the mean period, by $\approx 0.04\%$. In addition to the fundamental period, we were able to identify at least four distinct periods shown by specific dips over the full Sectors 18-59 dataset, including periods at 18.5683, 18.5672, 18.5473, and 18.5145 hr, with a typical measurement uncertainty of ≈ 0.0002 hr.

5. DISCUSSION

Quasiperiodicity—A periodic signal does not modulate; the CQVs are *quasiperiodic*. This is a qualitative departure from the “persistent” vs. “transient” flux dip distinction from Stauffer et al. (2017). While the dips can appear persistent over timescales of even up to 100 cycles, our view is that all the CQV dips seem to be transient over timescales of more than 1000 cycles (Figure 3).

With that said, one might expect a truly quasiperiodic process to be able to explore all phase angles with equal weight. LP 12-502, and many other CQVs, have preferred phases. For LP 12-502 for instance, all of the dips happen over a fixed phase duration of two thirds of the period. Phases between $\{0.45, 0.8\}$ are “out of limits” for any dipping material. We interpret this as evidence either that *a*) some aspect the stellar magnetic field is strongly asymmetric, and can generate and hold stellar prominences at corotation, but only over two thirds of the great circle, or *b*) there is a physical structure – for instance a disintegrating planetesimal swarm – that is distributed over an arc of about 240° .

Some CQVs require external occulters—(rehash Bodman2017 timescale arguments)

Each CQV a snowflake?—One intriguing aspect of staring at Figure 2 is that, even after rescaling the amplitudes, no two CQVs exhibit exactly identical light curve morphology. There are of course similarities.

TIC 272248916 and TIC 442571495 match.

Predicting the future, given the past—Figure 3 shows that for 21 CQVs that were observed roughly two years apart, 5 showed obvious signs of the phenomenon in one sector, and marginal or non-existence signs in the other. We emphasize that the periods themselves were usually stable to $< 0.1\%$. However, this shape evolution suggests that CQVs have a duty cycle of $\approx 75\%$.

Why would the prominence scenario tend toward corotation?—This is analogous to quiescent prominences on the Sun (Kuperus & Tandberg-Hanssen 1967).

If the prominence scenario is correct, why don’t stars in the Hyades and Praesepe show the phenomenon?—The prominence scenario, in a broad sense, argues that some intrinsic stellar pro-

cess is key for generating the CQV phenomenon. If this were true, then stars of identical mass, size, and rotation periods might be expected to show the phenomenon in equal number – irrespective of age. This is because the stellar dynamo is generated by fluid motions inside the star, which should be identical for stars of the same mass, size, and rotation period.

Between ages of ≈ 100 Myr (AB Dor, Pleiades, Psc-Eri) and ≈ 700 Myr (Praesepe and Hyades), a $0.3 M_\odot$ star will shrink by $\approx 10\%$, from $\approx 0.33 R_\odot$ to $\approx 0.29 R_\odot$ (CITE MIST). This is not a particularly drastic size change. Similarly, many M-dwarfs have similarly rapid rotation periods at 700 Myr as they do at 100 Myr (CITE Rebull2022); the mean population does show some evidence for spin-down after the PMS contraction finishes, but a large fraction of the population is still spinning more rapidly than the ≈ 2 day limit at which the CQV phenomenon becomes less common.

Broadly speaking – the absence of old CQVs in our view seems to be more plausibly linked to a gradual depletion of dusty detritus from the planet formation era than it does to the changing stellar properties as stars gradually finish their pre-main-sequence evolution, and then continue to spin rapidly for many hundreds of millions of years.

Connection to debris disk evolution—The concordance model for planet formation invokes the presence of an accretion disk. The disk is truncated (by what?) at the magnetospheric truncation radius, which happens to often coincidentally be at the Keplerian corotation radius. In such a scenario, planetesimals and boulders can migrate inward due to Type X migration (CITE), until they hit a “dust trap” at the inner wall (CITE eg Kama2009, and related). Support for this model comes from the rotation periods of classical and weak-lined T Tauri stars (CITE Rebull2018, 2019); from near-infrared interferometric observations that detect thermal emission from the disk wall (CITE CITE); and from the turn-over in the exoplanet orbital period distribution, which occurs around 5-10 days for FGK stars, and perhaps even closer-in for M-dwarfs (CITE Petigura2022, and CITE for M-dwarfs).

Broadly, the existence of a dust trap at the disk truncation radius might be expected to trap larger boulders as well. Once the disk loses the gas, what happens to those boulders? They are no longer shielded. We then enter a phase of mass loss. Perhaps that phase is what we are observing.

Connection to close-in exoplanets—Planet occurrence rate studies based on Kepler showed that around (early) M-dwarfs, there are ≈ 0.1 planets per star with sizes between $1-4 R_\oplus$ and orbital periods within 3 days (Dressing & Charbonneau 2015). TRAPPIST-1b, a rocky planet with an orbital period of 1.5 days is a possible example of this type of planet (CITE), though it orbits a very low-mass star ($0.08 M_\odot$).

The connection between the CQV phenomenon and these close-in exoplanets remains to be made. If the dust cloud model is correct, then assuming that the compact multiplanet resonant chains migrate to within $\approx 5-10$ stellar radii within the first 100 Myr (e.g. CITE IZIDORO), the dust clouds and the planets would coexist for a non-negligible time interval. Rocky planets this young likely still have molten global

magma oceans (e.g. CITE LICHTENBERG REVIEW), and would undergo significant outgassing and atmospheric escape. A scenario in which close-in rocky planets serve as a possible source of dust for the clouds is not entirely implausible, though it remains to be explored.

A planetesimal swarm at corotation seems unlikely—It is tempting to interpret certain features of the LP 12-502 light curve in this framework of a disintegrating planetesimal swarm. For instance, the complex in cycles 248–298 could be well-fit by a sharp leading edge that decays over $0.2 P$ (3.7 hours). The earlier complex, during cycles 248–264 (pre-state-switch), could be fit by a similar profile. There are two degenerate explanations for the small “wiggles” in the exponential decay. In one explanation, the decay timescale is fast ($\approx 0.03 P$), and there are up to five exocomets, superposed. In the other, there is only one main “launching body”, and the material it ejects either has some sub-structure, or else is passing across (and in synchronicity with) a star with heavily substructured starspots across its surface.

While the number of free parameters in this type of model is somewhat dizzying, we have no right to believe that nature need be simple. Every dip in the exocomet tail model would have as free parameters the dip phase, the duration (captured by an exponential decay timescale), and the dip depth. In detail, the impact parameter would also enter. Allotting four free parameters per dip yields up to 32 free parameters for the light curve at the most complicated times (assigning one exocomet per local minimum).

However there are two glaring issues with the disintegrating planetesimal swarm idea. First, a large number of the dips show asymmetries in the *wrong direction* relative to the naive expectation of a trailing comet tail. Dust forward scattering might be one possible way out; so too might invoking non-exponentially decaying dust distributions as a function of azimuth. Second, and perhaps more serious, the (unseen) planetesimals should be on *exactly periodic* orbits over observable timescales, on the presumption that the planetesimals would be massive enough to not feel any headwind or magnetic field. This is not what is observed; instead, every dip period that is observed to be distinct from the fundamental 18.5611 hr period is both short-lived, and unique. The fundamental 18.5611 hr period itself is itself associated with material at too many phases to arguably be tied to a single launching body. This suggests that the dust clumps must be much less massive than a 1–100 km sized planetesimal, and therefore more easily influenced by the stellar magnetic field, and events like flares.

Interpretation of the $T \lesssim 15$ dropoff—Our search sample included 35472 unique stars with $12 < T < 14$, versus 2045 unique stars with $15 < T < 16$. This helps clarify why our detected CPVs become less common toward fainter TESS magnitudes, despite the relative ease of their detectability, even at $15 < T < 16$. It is because the TESS 2-minute data are very incomplete at the faint end.

6. CONCLUSIONS

We report on the existence of 53 objects that showed complex quasiperiodic behavior over at least one TESS sector between July 2018 and Sep 2022. Our search for these objects was restricted to dwarf stars bright enough for 1% precision photometry with TESS over 1 hour ($T < 16$), that were red ($G_{\text{BP}} - G_{\text{RP}} < 1.5$) and within 150 pc of the Sun. These 53 bona fide CQVs are listed in Table ???. This table also includes an additional 17 candidate CQVs, whose designation is less certain.

Analyzing the light curves of these objects, we draw the following conclusions.

- CQVs are *quasiperiodic*. While the mean periods in our sample seem to remain fixed over the span of available observations, the light curve shapes themselves evolve, similar to rotating stars.
- The same CQV can show dips with very similar but clearly distinct periods. LP 12-502, for instance, showed dips with four distinct periods within $\pm 0.3\%$ of the fundamental period, sometimes simultaneous, and each lasting for up to 50 cycles.
- The CQV phenomenon persists for at least 150 Myr, based on the existence of CQVs in AB Dor, the Pleiades, and Psc-Eri. It may extend to even older ages, however the lack of detected CQVs in the Hyades and Praesepe suggest that the phenomenon is unique to the pre-main-sequence for M-dwarfs.
- CQVs evolve over timescales that are both secular (> 100 cycles) and impulsive (< 1 cycle). “State-switches” can cause dips to collapse instantaneously, and are often (but not exclusively) linked with observed optical flares. Dip growth however seems to happen over durations of at least ten cycles.
- The population-averaged duty cycle for CQVs seems to be $\approx 75\%$, based on the fraction of bona fide CQVs that “turned off” during TESS re-observations.

Many questions remain. After correcting for line-of-sight inclination, are most young M-dwarfs CQVs? What observational signatures distinguish the proposed models (Figure 1, bottom row)? What organizational regularities characterize the CQV as a class of variable star? What physically sets the extremes of the CQV population, such as the longest rotation periods, hottest stellar temperatures, and oldest stellar ages? And finally, what connections, if any, do CQVs have to topics such as stellar evolution, M-dwarf magnetic fields, debris disks, and close-in exoplanets? While we have tried to point out possible connections, the most likely path toward definitive resolutions would be to observe a full phase curve of LP 12-502, or perhaps some other suitable object, using JWST/MIRI.

ACKNOWLEDGMENTS

This work was supported by the Heising-Simons 51 Pegasi b Fellowship (LGB) TIC 402980664 was observed at 120-second cadence thanks to the TESS Guest Investigator programs G022252 (PI: J. Schlieder; Sectors 18, 19, 25, 26) and G04168 (PI: R. Jayaraman; Sector 53).

author contribution statement goes here L.G.B. and R. J. conceived the project and executed the dip-based and Fourier-based searches, respectively. L.G.B. drafted the initial manuscript, and performed the cluster membership analysis. S. R. and R. J. vetted the results from the Fourier search.

L.A.H. contributed to project design. All authors assisted in manuscript revision.

Software: astrobase (Bhatti et al. 2021), lightkurve (Lightkurve Collaboration et al. 2018), scipy (Virtanen et al. 2020), TESS-point (Burke et al. 2020),

Facilities: *Astrometry*: Gaia (Gaia Collaboration et al. 2018,?). *Imaging*: Second Generation Digitized Sky Survey. *Spectroscopy*: Keck:I (HIRES; Vogt et al. 1994). *Photometry*: TESS (Ricker et al. 2015), *Broadband photometry*: 2MASS (CITE). APASS (CITE). Gaia (Gaia Collaboration et al. 2018,?). Pan-STARRS1 (CITE). SDSS (CITE). AllWISE (CITE).

REFERENCES

- Allard, F., Homeier, D., & Freytag, B. 2012, Philosophical Transactions of the Royal Society A: Mathematical, Physical and Engineering Sciences, 370, 2765
- Ansdell, M., Gaidos, E., Rappaport, S. A., et al. 2016, *ApJ*, 816, 69
- Asplund, M., Grevesse, N., Sauval, A. J., & Scott, P. 2009, *ARA&A*, 47, 481
- Bailer-Jones, C. A. L., Rybizki, J., Fouesneau, M., Demleitner, M., & Andrae, R. 2021, *AJ*, 161, 147
- Barber, R. J., Tennyson, J., Harris, G. J., & Tolchenov, R. N. 2006, *MNRAS*, 368, 1087
- Basri, G. 2021, An Introduction to Stellar Magnetic Activity
- Bhatti, W., Bouma, L., Joshua, et al. 2021, waqasbhatti/astrobase: astrobase v0.5.3, Zenodo
- Bodman, E. H. L., Quillen, A. C., Ansdell, M., et al. 2017, *MNRAS*, 470, 202
- Bouma, L. G., Winn, J. N., Ricker, G. R., et al. 2020, *AJ*, 160, 86
- Bouma, L. G., Curtis, J. L., Masuda, K., et al. 2022, *AJ*, 163, 121
- Boyle, A. W., & Bouma, L. G. 2022, arXiv e-prints, arXiv:2211.09822
- Bressan, A., Marigo, P., Girardi, L., et al. 2012, *MNRAS*, 427, 127
- Brogi, M., Keller, C. U., de Juan Ovelar, M., et al. 2012, *A&A*, 545, L5
- Burke, C. J., Levine, A., Fausnaugh, M., et al. 2020, TESS-Point: High precision TESS pointing tool, Astrophysics Source Code Library, record ascl:2003.001
- Cantat-Gaudin, T., Anders, F., Castro-Ginard, A., et al. 2020, *A&A*, 640, A1
- Capistrant, B. K., Soares-Furtado, M., Vanderburg, A., et al. 2022, *ApJS*, 263, 14
- Chen, Y., Girardi, L., Bressan, A., et al. 2014, *MNRAS*, 444, 2525
- Cody, A. M., Stauffer, J., Baglin, A., et al. 2014, *AJ*, 147, 82
- David, T. J., & Hillenbrand, L. A. 2015, *ApJ*, 804, 146
- Dressing, C. D., & Charbonneau, D. 2015, *ApJ*, 807, 45
- Fausnaugh, M., Morgan, E., Vanderspek, R., et al. 2021, *PASP*, 133, 095002
- Feiden, G. A. 2016, *A&A*, 593, A99
- Gagné, J., Mamajek, E. E., Malo, L., et al. 2018, *ApJ*, 856, 23
- Gaia Collaboration, Brown, A. G. A., Vallenari, A., et al. 2018, *A&A*, 616, A1
- Gully-Santiago, M. A., Herczeg, G. J., Czekala, I., et al. 2017, *ApJ*, 836, 200
- Günther, M. N., Berardo, D. A., Ducrot, E., et al. 2022, *AJ*, 163, 144
- Hippke, M., David, T. J., Mulders, G. D., & Heller, R. 2019, *AJ*, 158, 143
- Jenkins, J. M., Twicken, J. D., McCauliff, S., et al. 2016, in Society of Photo-Optical Instrumentation Engineers (SPIE) Conference Series, Vol. 9913, Software and Cyberinfrastructure for Astronomy IV, ed. G. Chiozzi & J. C. Guzman, 99133E
- Kerr, R. M. P., Rizzuto, A. C., Kraus, A. L., & Offner, S. S. R. 2021, *ApJ*, 917, 23
- Koen, C. 2021, *MNRAS*, 500, 1366
- . 2023, *MNRAS*, 518, 2921
- Kuperus, M., & Tandberg-Hanssen, E. 1967, *SoPh*, 2, 39
- Lightkurve Collaboration, Cardoso, J. V. d. M., Hedges, C., et al. 2018, Lightkurve: Kepler and TESS time series analysis in Python, Astrophysics Source Code Library, record ascl:1812.013
- Meingast, S., Alves, J., & Rottensteiner, A. 2021, *A&A*, 645, A84
- Palumbo, E. K., Montet, B. T., Feinstein, A. D., et al. 2022, *ApJ*, 925, 75
- Pecaut, M. J., & Mamajek, E. E. 2013, *ApJS*, 208, 9
- Popinchalk, M., Faherty, J. K., Curtis, J. L., et al. 2023, *ApJ*, 945, 114
- Rajpurohit, A. S., Reylé, C., Allard, F., et al. 2013, *A&A*, 556, A15
- Rappaport, S., Levine, A., Chiang, E., et al. 2012, *ApJ*, 752, 1
- Ratzenböck, S., Meingast, S., Alves, J., Möller, T., & Bomze, I. 2020, *A&A*, 639, A64
- Rebull, L. M., Stauffer, J. R., Cody, A. M., et al. 2018, *AJ*, 155, 196
- Rebull, L. M., Stauffer, J. R., Bouvier, J., et al. 2016, *AJ*, 152, 114

- Ricker, G. R., Winn, J. N., Vanderspek, R., et al. 2015, *Journal of Astronomical Telescopes, Instruments, and Systems*, 1, 014003
- Robinson, C. E., Espaillat, C. C., & Owen, J. E. 2021, *ApJ*, 908, 16
- Rodriguez, D. R., van der Plas, G., Kastner, J. H., et al. 2015, *A&A*, 582, L5
- Sanderson, H., Jardine, M., Collier Cameron, A., Morin, J., & Donati, J. F. 2023, *MNRAS*, 518, 4734
- Somers, G., Cao, L., & Pinsonneault, M. H. 2020, *ApJ*, 891, 29
- Speagle, J. S. 2020, *MNRAS*, 493, 3132
- Stassun, K. G., Kratter, K. M., Scholz, A., & Dupuy, T. J. 2012, *ApJ*, 756, 47
- Stassun, K. G., Oelkers, R. J., Pepper, J., et al. 2018, *AJ*, 156, 102
- Stauffer, J., Collier Cameron, A., Jardine, M., et al. 2017, *AJ*, 153, 152
- Stauffer, J., Rebull, L., David, T. J., et al. 2018, *AJ*, 155, 63
- Stellingwerf, R. F. 1978, *ApJ*, 224, 953
- Vanderburg, A., Johnson, J. A., Rappaport, S., et al. 2015, *Nature*, 526, 546
- Vines, J. I., & Jenkins, J. S. 2022, *MNRAS*, 513, 2719
- Virtanen, P., Gommers, R., Oliphant, T. E., et al. 2020, *Nature Methods*, 17, 261
- Vogt, S. S., Allen, S. L., Bigelow, B. C., et al. 1994, in *Society of Photo-Optical Instrumentation Engineers (SPIE) Conference Series*, Vol. 2198, *Instrumentation in Astronomy VIII*, ed. D. L. Crawford & E. R. Craine, 362
- Waugh, R. F. P., & Jardine, M. M. 2022, *MNRAS*, 514, 5465
- Winn, J. N. 2010, in *Exoplanets*, ed. S. Seager, 55
- Zhan, Z., Günther, M. N., Rappaport, S., et al. 2019, *ApJ*, 876, 127
- Zieba, S., Zwintz, K., Kenworthy, M. A., & Kennedy, G. M. 2019, *A&A*, 625, L13
- Zuckerman, B. 2019, *ApJ*, 870, 27

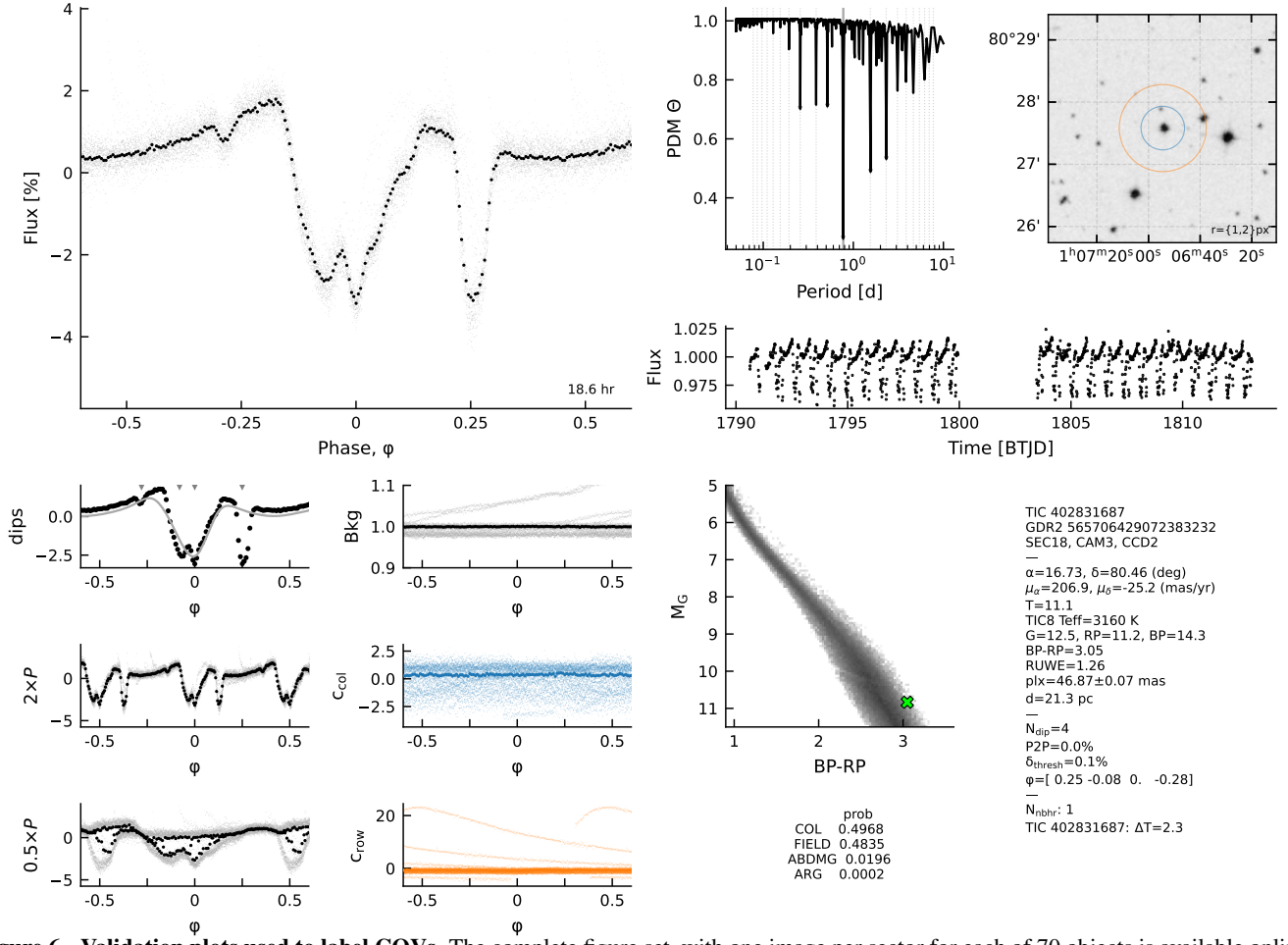


Figure 6. Validation plots used to label CQVs. The complete figure set, with one image per sector for each of 70 objects is available online. Panels are as follows. *a*): Phase-folded light curve; gray points are raw 2-minute data and black points are binned to 200 points per cycle. *b*): Phase-dispersion minimization (PDM) periodogram. Dotted lines show up to the 10th harmonic and subharmonic. *c*): DSS finder chart, with 1- and 2-TESS pixel radius circles displayed for scale. *d*): Cleaned light curve, binned to 20-minute cadence, in Barycentric TESS Julian Date (BTJD). *e*): Phase-folded light curve, binned to 100 points per cycle. The gray line denotes the automated spline-fit to the wrapped phase-folded light curve, and small gray triangles denote automatically identified local minima. *f*): Phase-folded light curve at twice the peak period. *g*): Phase-folded light curve at half the peak period. *h*): Phase-folded time-series within the “background” aperture defined in the SPOC light curves. *i*): Phase-folded flux-weighted centroid in the column direction. *j*): Phase-folded flux-weighted centroid in the row direction. *k*): Gaia DR2 color–absolute magnitude diagram. *l*): Information from Gaia DR2, TIC8, and the automated dip-counting search pipeline. “Neighbors”, abbreviated “nbhr”, are listed within apparent distances of 2 TESS pixels if $\Delta T < 2.5$. *m*): BANYAN- Σ v1.2 association probabilities, calculated using positions, proper motions, and the parallax.

APPENDIX

A. VALIDATION PLOTS

Figure 6 shows the type of plot used to visually assess whether a source was likely to be a CQV, eclipsing binary, or simply a rapidly rotating star.

B. LP 12-502

The light curve— Figure 4 shows an alternative view of the LP-502 light curve from Figure 5, split into successive TESS orbits. We binned the light curve to 15-minute intervals for visual clarity, and required at least one (120-second cadence) flux measurement per bin. Points more than 2.5σ above the median are drawn in gray, also for visual clarity. Missing data are not

drawn (a common plotting error when “drawing” light curves, rather than showing a scatter plot). The red lines point to specific state switches, discussed elsewhere in the text.

Figure 7 shows another alternative view of Figure 5, but arranged to enable easy visual appreciation of transit timing changes, rather than transit depth changes. A best-fitting two-harmonic sinusoid has been independently fitted and subtracted from the Sector 18-19 data, 25-26 data, and 53, 58, and 59 data.

Finally, Figure 8 shows “river plots” of the same data, split into very similar intervals: the Sector 18-19 data, 25-26 data, 53 data, and 58-59 data. State changes are evident in these plots whenever there is a sudden change in color. **todo: fix missing data to be different from the flare color**

C. NO ADDITIONAL POWER AT 20 SECOND CADENCE

Going from K2 to TESS, an important discovery was that the CQV shapes can significantly evolve, since the stars can vary over timescales of just a few minutes. We observed a set of CQVs between 2020 and 2021 using the TESS 20-second cadence mode (TESS DDT029). **todo: list the stars. todo: examine the 2min vs 20sec periodograms, and summarize in a few sentences whether any difference is there.**

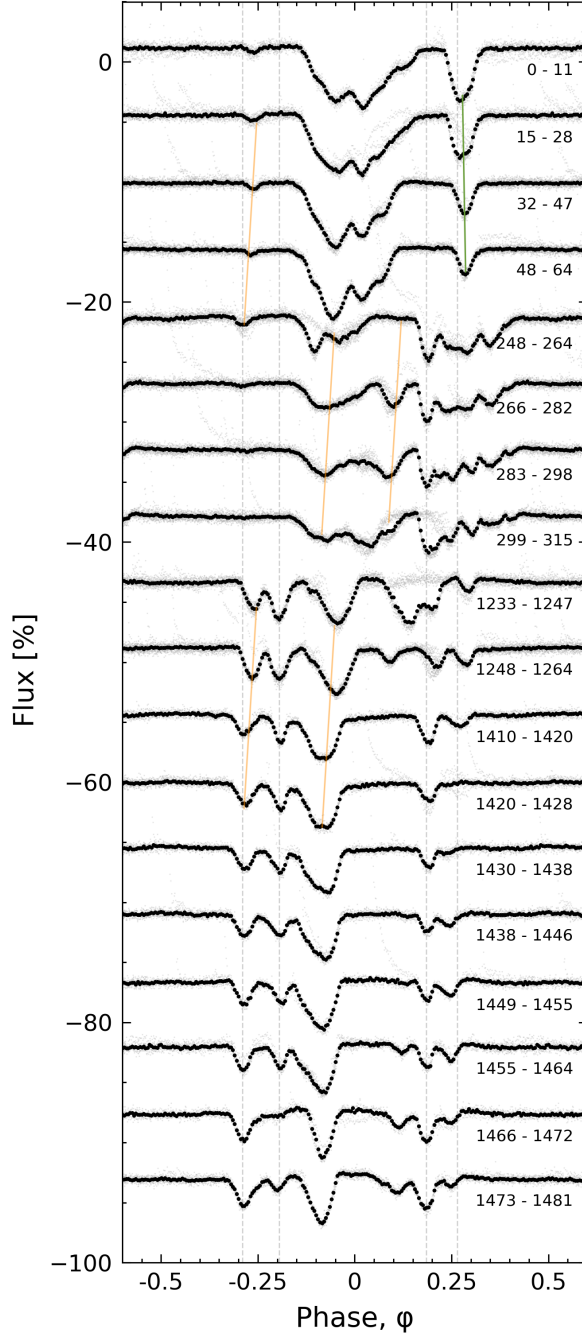


Figure 7. Alternative view of the evolution of LP 12-502 (Figure 5), arranged to emphasize changes in transit times. There are 200 binned black points per cycle; a two-harmonic sinusoid has been subtracted over specific chunks in time (see text). Vertical gray lines are underplotted to help guide the eye to instances in which preferred dip phases synchronize over long baselines. The orange and green lines guide the eye to where dips appear to change the positions of their local minima.

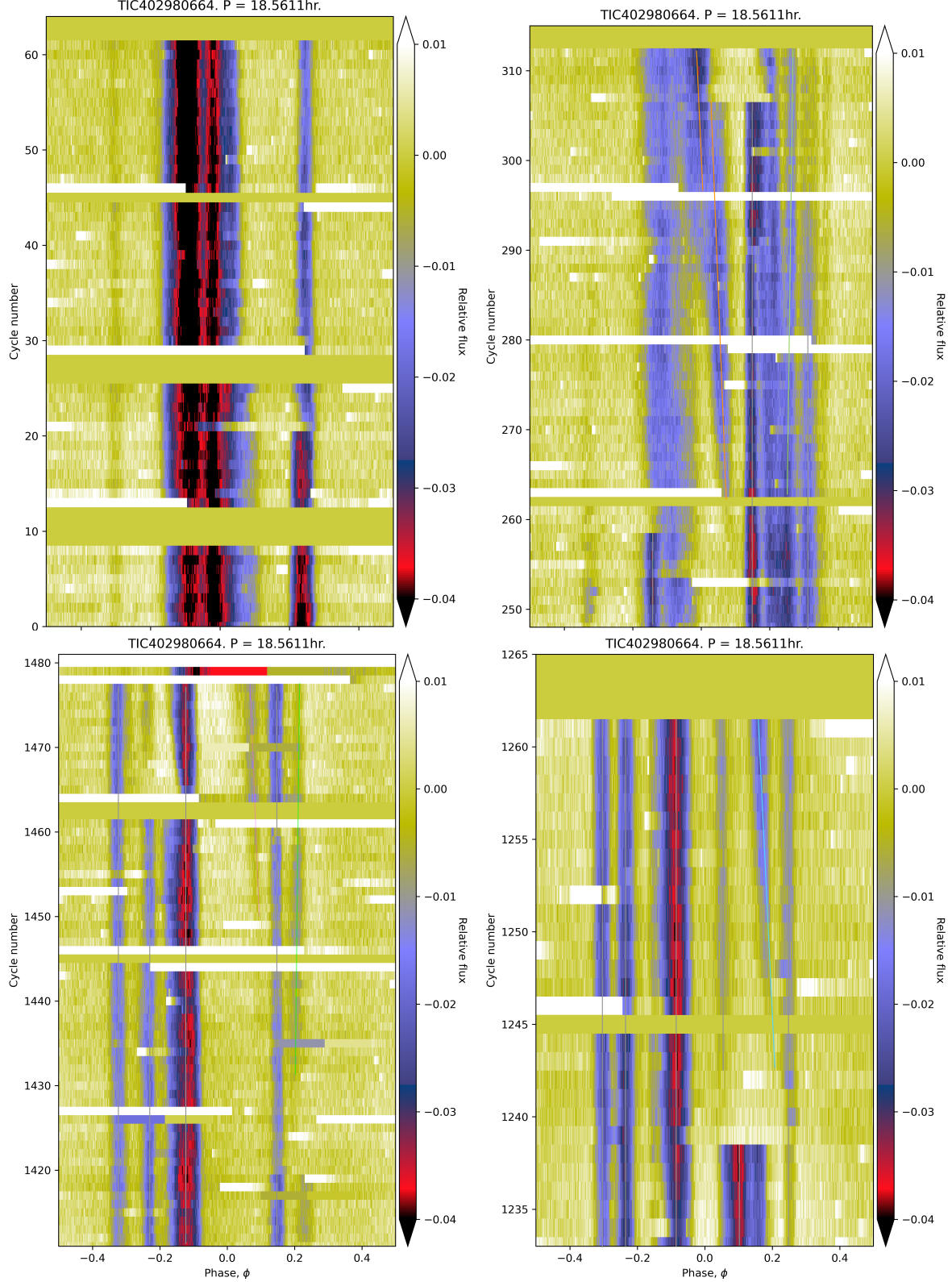


Figure 8. River plots of LP 12-502, showing (clockwise from top-left) Sectors 18-19, 25-26, 53, and 58-59. A two-harmonic sinusoid has been subtracted over specific chunks in time (see text). For Sectors 25-26 (cycles 248-315), three periods are overplotted: $P=18.5611\text{ hr}$ (gray vertical line); 18.5404 hr (orange); 18.5683 hr (green). For Sector 53, gray is identical, while cyan is 18.5145 hr . For Sectors 58-59, the magenta line is 18.5473 hr , and the green line is 18.5672 hr .